Continental Shelf Research 272 (2024) 105149

Contents lists available at ScienceDirect

Continental Shelf Research

journal homepage: www.elsevier.com/locate/csr

The effect of alongshore wind stress on a buoyancy current's stability

K.H. Brink

Department of Physical Oceanography, Mail Stop 21, Woods Hole Oceanographic Institution, Woods Hole, MA, 02543, USA

ARTICLE INFO

Keywords:
Buoyancy current
Baroclinic instability
Wind forcing
Eddy energy

ABSTRACT

Buoyancy fronts reach from the surface to the bottom over continental shelves, separating light inshore water from denser offshore water, and are known to be responsive to Ekman transport (and associated return flow at depth) driven by alongshore winds. The consequent changes in frontal structure are clearly related to changes in the gravitational Available Potential Energy (*APE*), so it is reasonable to expect that these winds will affect the eddy field that results from baroclinic instabilities. Idealized numerical experiments and scaling analyses are brought to bear on this problem. It is found that several days of wind-driven downwelling (which creates more nearly vertical isopycnals) generally leads to an enhancement in the time maximum of volume-averaged Eddy Kinetic Energy (*EKE*). Upwelling-favorable winds (which tend to flatten isopycnals) usually lead to a decrease in *APE*, hence in eddy energy. The exception to this rule occurs when the winds are strong enough that an upwelling front forms inshore of the buoyant water, in which case *APE* and *EKE* may increase.

1. Introduction

Estuarine buoyant outflows generally lead to a relatively fresh current over the shelf, flowing alongshore in the direction of free long coastal-trapped wave propagation. The offshore boundary of such a current often takes the form of a surface-to-bottom front (called a "buoyancy front" in the following). These fronts are known to be baroclinically unstable, and they have been studied in a sequence of increasingly realistic models over the decades, beginning with linear stability calculations (e.g., Flagg and Beardsley, 1978), laboratory experiments (e.g., Griffths and Linden, 1981) and increasingly sophisticated numerical studies that deal with finite amplitudes and an evolving eddy field (e.g., Rogers-Cotrone et al., 2008; Zhang and Gawarkiewicz, 2015; Hetland, 2017; Chen et al., 2019). Quantitative observational evidence for baroclinic instabilities in buoyancy currents is not very abundant, given the complex ways in which these currents respond to winds and other forcings, but Weingartner et al. (1999) do provide such information for the shelf north of Siberia.

There are ample observations demonstrating that alongshore winds affect buoyancy currents and their fronts, e.g., off Chesapeake Bay (Lentz and Largier, 2006), in the Gulf of Maine (Fong et al., 1997), in the Columbia River outflow (Hickey et al., 1998) and off Delaware Bay (Sanders and Garvine, 2001). Simple two-dimensional (cross-shelf and vertical) coastal models account for many aspects of the wind response. (Here, "coastal" is taken to mean that there is a lateral boundary and a sloping bottom.) Lentz (2004), for example, shows that an upwelling-favorable alongshore wind stress stretches out the front in the cross-shelf direction and dilutes the buoyant waters through vertical mixing. The net result would be an overall more gently sloping front and hence a decrease in gravitational Available Potential Energy (*APE*, which can be thought of as a measure of overall isopycnal tilting). Alternatively, Moffat and Lentz (2012) show that downwelling-favorable winds lead to a steepening of the front and the establishment of separate cross-shelf/vertical circulation cells onshore and offshore of the front. The steepening equates to an increase in *APE*. Thus, to the extent that *APE* is a predictor of Eddy Kinetic Energy (*EKE*), it seems probable that alongshore winds could have a substantial effect on the *EKE* of a baroclinically unstable system. Indeed, Rogers-Cotrone et al. (2008) hint that this may be the case by showing that winds affect the offshore freshwater eddy flux.

There exist some interesting contributions concerning the effect of along-frontal winds in the open ocean (e.g., Thomas and Lee, 2005; Thomas and Taylor, 2010). While these are very useful in terms of understanding isolated fronts, they do not completely apply to a coastal setting for a couple of reasons. Most importantly, the coastal boundary means that a two-dimensional configuration must conserve volume by having a subsurface cross-shelf flow that is equal and opposite to the surface Ekman transport. This deeper flow can create important density gradients and, if the water is sufficiently shallow (say 100 m or less in a coastal context), this counterflow can be comparable in magnitude to the near-surface cross-shelf velocity. Second, in a coastal context, the bottom slope is an important factor, especially in terms of how it affects

E-mail address: kbrink@whoi.edu.

https://doi.org/10.1016/j.csr.2023.105149
Received 13 January 2023; Received in revised form 13 November 2023; Accepted 19 November 2023
Available online 3 December 2023

instability, e.g., Blumsack and Gierasch (1972), Hetland (2017). Specifically, when the isopycnal slope has the opposite sign to the bottom slope, linear instabilities grow more slowly and in a narrower wavenumber range than when the bottom is flat. If the isopycnal slope has the same sign as the bottom slope, instabilities can grow faster than for a flat bottom case, but too strong a slope leads to stability.

Some aspects of buoyancy frontal instability have been treated capably in the literature already, notably Spall and Thomas (2016) who concentrate on water mass formation associated with sustained wind-driven vertical mixing acting on the eddy field resulting from frontal baroclinic instability. In contrast, the present contribution deals with the influence of short-lived (several days duration) alongshore winds, hence upwelling and downwelling, on frontal stability, hence eddy formation itself. As such, multiple idealized numerical model runs are executed, and scaling analysis is conducted to characterize the wind's effect on ultimate *EKE* and on the alongshore eddy scale.

2. Methodology

2.1. Calculations

All calculations presented here make use of the hydrostatic, primitive equation ROMS model system (e.g., Haidvogel et al., 2000). Specifically, the equations to be solved are

$$u_t + uu_x + vu_y + wu_z - fv = -\frac{1}{\rho_0}p_x + (D_V u_z)_z, \tag{2.1a}$$

$$v_t + uv_x + vv_y + wv_z + fu = -\frac{1}{\rho_0}p_y + (D_V v_z)_z, \tag{2.1b}$$

$$0 = -p_z - g\rho, \tag{2.1c}$$

$$u_x + v_y + w_z = 0, \tag{2.1d}$$

$$\rho_t + u\rho_x + v\rho_y + w\rho_z = (B_V \rho_z)_z, \tag{2.1e}$$

and

$$\rho = \rho_0[1 - \mu(T - T_0)]\ . \tag{2.1f}$$

The velocity components (u, v, w) are in the x (offshore), y (alongshore) and z (vertical) directions respectively. Time is t. The constant background density is ρ_0 (=1027 kg/m^3), while the variable density is ρ. Pressure is p, the temperature is T, the Coriolis parameter is f, the acceleration due to gravity is g and the thermal expansion coefficient is μ (=1.7×10^{-4} 1/°C). Subscripted independent variables represent partial differentiation. The eddy viscosity D_V and eddy diffusivity B_V are found using the Mellor-Yamada level 2.5 turbulence closure scheme (e.g., Wijesekera et al., 2003). The bottom stress $\boldsymbol{\tau_B}$ is linearly proportional to near-bottm velocity $\boldsymbol{v_B}$:

$$\boldsymbol{\tau_B} = \rho_0 r \boldsymbol{v_B} \tag{2.2}$$

where r is a bottom resistance coefficient and bold characters represent horizontal vectors. No explicit horizontal mixing or friction is applied.

The numerical experiments all begin with a tilting (slope γ) surface-to bottom front of width Δx in an ocean with otherwise constant stratification (vertical temperature gradient Γ). Specifically (Fig. 1a),

$$T = T_1 + \Gamma z \text{ for } x < x_F + z/\gamma \tag{2.3a}$$

$$T = T_1 + \Gamma z + (T_2 - T_1)\frac{1}{2}\left\{1 - \cos\left[\frac{\pi(x - x_F) - z/\gamma}{\Delta x}\right]\right\} \tag{2.3b}$$
$$\text{for } x_F + z/\gamma < x < x_F + \Delta x + z/\gamma$$

$$T = T_2 + \Gamma z \text{ for } x > x_F + \Delta x + z/\gamma \tag{2.3c}$$

T_1 and T_2 are the surface temperatures inshore and offshore of the front respectively so the frontal temperature contrast $\Delta T = T_1 - T_2 > 0$. The initial cross-shelf velocity is zero, and the initial alongshore velocity and sea level elevation are in thermal wind balance with (2.3) such that velocity at the bottom is zero (consistent with Chapman and Lentz, 1994). The water depth h always has the form

$$h = h_0 + \alpha x \tag{2.4}$$

for $x < 75$ km, where $h_0 = 5$ m, and the depth is constant for larger x.

An alongshore wind stress is imposed during the early part of each model run:

$$\tau_0^y = \frac{1}{2}\left[1 - \cos\left(\frac{\pi t}{t_R}\right)\right]\tau_A \text{ for } t < t_R \tag{2.5a}$$

$$\tau_0^y = \tau_A \text{ for } t_R < t < t_1 \tag{2.5b}$$

$$\tau_0^y = \frac{1}{2}\left\{1 + cos\left[\frac{\pi(t - t_1)}{t_R}\right]\right\} \text{ for } t_1 < t < t_1 + t_R \tag{2.5c}$$

$$\tau_0^y = 0 \text{ for } t > t_1 + t_R\ . \tag{2.5d}$$

The ramp time t_R is always 1 day. The effect of this wind stress is either to flatten out the front when the winds are upwelling favorable (i.e. when $\tau_A > 0$: Fig. 1b, see Lentz, 2004) or to steepen the front when winds are downwelling favorable (i.e., when $\tau_A < 0$: Fig. 1c, see Moffat and Lentz, 2012).

The model domain is cyclic in the alongshore direction (channel length of 128 km), and the grid extends to 100 km offshore. Horizontal grid resolution is 0.16 km in both the alongshore and cross-shelf directions, while there are 36 levels in the vertical. At the offshore boundary, a no-normal-gradient condition is used for both velocity

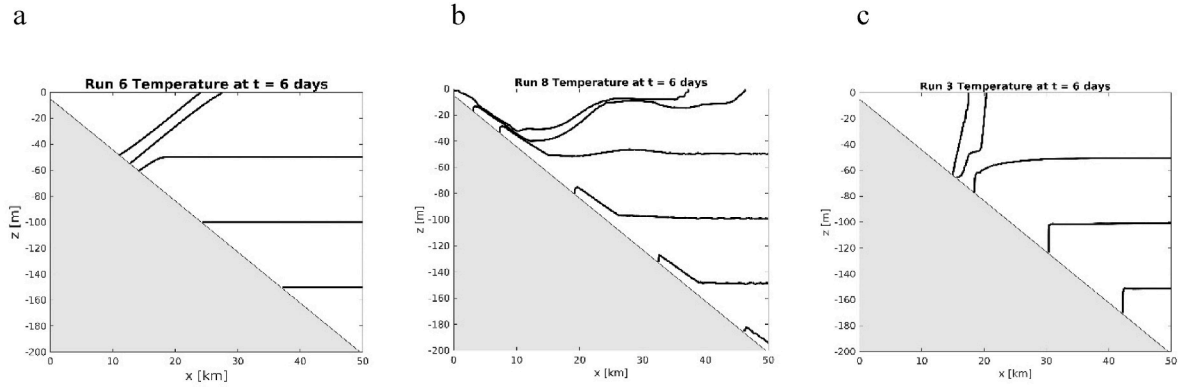

Fig. 1. Cross sections of temperature at $t = 6$ days, immediately after the wind stress ceases and before there is substantial growth of instabilities. Calculated for runs 6, 8 and 3. The contour interval is 1 °C. a) No wind stress, b) upwelling-favorable wind stress, c) downwelling-favorable wind stress.

components, and a radiation condition is used for both free surface height and temperature. In addition, temperature at the boundary is nudged back to its initial state with a time constant of 10 days.

A total of 44 numerical experiments were conducted (Table 1). Among the properties varied were the strength and direction of the alongshore wind stress τ_A, the initial cross-frontal temperature contrast (ΔT), the Coriolis parameter f, the frontal slope γ, the bottom slope α, the initial ambient stratification Γ, the frontal width Δx, the offshore location of the front x_F, and the bottom resistance parameter r. The runs are grouped in Table 1 so that within each cluster, the wind stress is the only quantity that changes.

2.2. Diagnostics

For the purpose of diagnostic calculations, all fields are broken into an along-channel mean (denoted by curly brackets: { }) and a deviation from it: the eddy component (denoted by a prime: '). Thus, for variable q

$$q = \{q\}(x,z,t) + q'(x,y,z,t)\ . \tag{2.6}$$

The mean kinetic energy per unit mass is then

$$mke(x,z,t) = \left[\{u\}^2 + \{v\}^2\right]/2 \tag{2.7a}$$

while the eddy kinetic energy per unit mass is

Table 1
Description of model runs.

Run	F × 10^4	α × 10^3	r × 10^4	x_F	Δx	γ × 10^3	ΔT	Γ	τ_A	t_1	EKE_M × 10^3	λ	APE_R × 10^3	C^ρ × 10^3	C^x × 10^3	C^z × 10^3
	1/s		m/s	km	km		°C	°C/m	N/m^2	days	m^2/s^2	km	m^2/s^2	m^2/s^2	m^2/s^2	m^2/s^2
1	1.0	3.933	5.	20.	8.	5.	2.	0.02	−0.08	5.0	1.473	23.6	11.55	15.64	1.08	2.52
2	1.0	3.933	5.	20.	8.	5.	2.	0.02	−0.06	5.0	1.523	26.8	10.82	9.50	0.47	1.97
3	1.0	3.933	5.	20.	8.	5.	2.	0.02	−0.04	5.0	1.708	17.6	9.69	7.43	0.28	1.35
4	1.0	3.933	5.	20.	8.	5.	2.	0.02	−0.03	5.0	1.667	21.2	8.92	7.00	−0.10	0.90
5	1.0	3.933	5.	20.	8.	5.	2.	0.02	−0.02	5.0	1.434	19.6	7.94	6.10	−0.25	0.78
6	1.0	3.933	5.	20.	8.	5.	2.	0.02	0	5.0	1.408	21.2	5.38	3.31	0.83	0.29
7	1.0	3.933	5.	20.	8.	5.	2.	0.02	0.02	5.0	1.338	18.4	3.35	1.72	0.35	0.17
8	1.0	3.933	5.	20.	8.	5.	2.	0.02	0.04	5.0	1.168	17.6	3.66	2.16	−0.20	0.24
9	1.0	3.933	5.	20.	8.	5.	3.	0.02	−0.04	5.0	2.117	24.8	13.98	11.15	−0.25	2.66
10	1.0	3.933	5.	20.	8.	5.	3.	0.02	0	5.0	1.869	26.0	8.70	4.58	2.42	1.26
11	1.0	3.933	5.	20.	8.	5.	3.	0.02	0.04	5.0	1.886	18.4	4.75	2.48	0.08	0.39
12	0.5	3.933	5.	20.	8.	5.	2.	0.02	−0.04	5.0	1.705	41.6	9.52	10.28	−0.13	1.14
13[a]	0.5	3.933	5.	20.	8.	5.	2.	0.02	0	5.0	1.848	36.8	5.38	2.54	2.66	1.24
14[a]	0.5	3.933	5.	20.	8.	5.	2.	0.02	0.04	5.0	0.990	52.0	3.07	−0.45	0.69	0.14
15	1.0	3.933	5.	20.	8.	2.5	2.	0.02	−0.04	5.0	0.982	17.6	6.63	4.88	0.15	0.96
16	1.0	3.933	5.	20.	8.	2.5	2.	0.02	0	5.0	0.591	20.8	2.79	1.30	−0.27	0.04
17	1.0	3.933	5.	20.	8.	2.5	2.	0.02	0.02	5.0	0.529	21.2	1.70	0.90	−0.03	0.07
18	1.0	3.933	5.	20.	8.	10.	2.	0.02	−0.04	5.0	2.065	22.4	12.67	10.45	0.62	1.24
19	1.0	3.933	5.	20.	8.	10.	2.	0.02	0	5.0	1.997	25.2	8.23	4.80	1.88	0.87
20	1.0	3.933	5.	20.	8.	10.	2.	0.02	0.02	5.0	1.886	20.0	5.95	2.45	0.12	0.21
21	1.0	3.933	5.	20.	8.	10.	2.	0.02	0.04	5.0	2.160	18.4	4.90	2.62	0.56	0.45
22	1.0	6.6	5.	20.	8.	5.	2.	0.02	−0.04	5.0	2.371	28.0	8.48	6.87	0.43	1.37
23	1.0	6.6	5.	20.	8.	5.	2.	0.02	0	5.0	1.658	31.2	4.89	3.34	0.89	0.38
24	1.0	6.6	5.	20.	8.	5.	2.	0.02	0.04	5.0	0.726	24.8	2.84	1.84	−0.19	−0.21
25	1.0	3.933	5.	20.	8.	5.	2.	0.01	−0.04	5.0	1.105	22.0	9.78	7.65	1.01	1.58
26	1.0	3.933	5.	20.	8.	5.	2.	0.01	0	5.0	1.075	17.6	6.03	3.33	0.75	0.38
27	1.0	3.933	5.	20.	8.	5.	2.	0.01	0.04	5.0	1.031	15.6	3.12	1.48	0.11	0.13
28	1.0	3.933	5.	20.	8.	5.	2.	0.04	−0.04	5.0	1.842	21.6	9.19	7.78	0.32	1.14
29	1.0	3.933	5.	20.	8.	5.	2.	0.04	0	5.0	1.271	28.0	4.32	2.80	0.35	0.32
30	1.0	3.933	5.	20.	8.	5.	2.	0.04	0.04	5.0	1.061	21.2	3.70	2.62	−0.86	−0.21
31	1.0	3.933	5.	20.	16.	5.	2.	0.02	−0.04	5.0	2.15	27.6	12.01	10.97	−0.55	1.45
32	1.0	3.933	5.	20.	16.	5.	2.	0.02	0	5.0	1.951	27.6	6.20	3.64	0.48	0.02
33	1.0	3.933	5.	20.	16.	5.	2.	0.02	0.04	5.0	1.522	18.8	3.95	2.26	0.11	0.01
34	1.0	3.993	5.	10.	8.	5.	2.	0.02	−0.04	5.0	0.358	12.8	3.59	2.97	−0.04	0.45
35	1.0	3.933	5.	10.	8.	5.	2.	0.02	0	5.0	0.310	14.4	1.75	1.03	0.03	0.08
36	1.0	3.933	5.	10.	8.	5.	2.	0.02	0.04	5.0	0.379	19.2	2.59	1.39	−0.13	−0.11
37	1.0	3.933	1.	20.	8.	5.	2.	0.02	−0.04	5.0	1.317	26.0	9.19	3.41	0.60	0.52
38	1.0	3.933	1.	20.	8.	5.	2.	0.02	0	5.0	1.325	18.0	5.38	2.26	0.74	0.36
39	1.0	3.933	1.	20.	8.	5.	2.	0.02	0.04	5.0	1.151	15.6	4.00	1.91	0.02	0.22
40	1.0	3.933	20.	20.	8.	5.	2.	0.02	−0.04	5.0	1.436	21.6	9.80	7.52	−0.24	1.09
41	1.0	3.933	20.	20.	8.	5.	2.	0.02	0	5.0	1.188	23.2	5.38	3.38	0.53	0.34
42	1.0	3.933	20.	20.	8.	5.	2.	0.02	0.04	5.0	1.038	18.4	3.17	1.73	0.02	0.10
43	1.0	3.933	5.	24.	8.	5.	2.	0.02	0.02	10.0	1.196	17.2	4.20	2.32	−0.10	0.15
44	1.0	3.933	5.	24.	8.	5.	2.	0.02	0	5.0	1.683	28.0	6.82	4.02	0.69	0.41

[a] Runs where barotropic instability dominates over baroclinic. Not used to evaluate the scalings of section 4.

$$eke(x,z,t) = \left[\{u'^2\} + \{v'^2\}\right]/2 \tag{2.7b}$$

and the potential energy per mass (averaged alongshore) due to the density field is

$$pe(x,z,t) = \{g\rho z\}/\rho_0\ . \tag{2.7c}$$

Note that the form of (2.7c) makes it difficult to define an eddy potential energy unless further approximations are made. In the following, the potential energy associated with the free surface displacement is ignored, consistent with the rigid lid approximation (i.e., assuming that $L^2f^2/(gH)$ is small where H and L are representative horizontal and vertical length scales, respectively), an assumption that is well justified in all of the present model runs.

These diagnostics are summarized by averaging over the cross-sectional area inshore of $x = W$ (where $W = 40$ km). Thus

$$A = \int_0^W \int_{-h}^0 dzdx \tag{2.8a}$$

The area-averaged mean kinetic energy per unit mass is then

$$MKE(t) = \frac{1}{2A}\int_0^W \int_{-h}^0 \left(\{u\}^2 + \{v\}^2\right)dzdx, \tag{2.8b}$$

the area-averaged eddy kinetic energy per unit mass is

$$EKE(t) = \frac{1}{A}\int_0^W \int_{-h}^0 eke\ dzdx, \tag{2.8c}$$

and the area-averaged potential energy per unit mass is

$$PE(t) = \frac{1}{\rho_0 A}\int_0^W \int_{-h}^0 \{g\rho z\}dzdx\ . \tag{2.8d}$$

The available potential energy *APE* is estimated by first rearranging the three-dimensional density field so that all density surfaces are flat while the mass and volume are conserved. This density field's *PE* is then subtracted from the actual field to get the *APE*.

Of great interest are the conversions among the different energy pools. For example, the conversion from potential to kinetic energy is given by

$$C_{PE\to KE} = -\frac{g}{\rho_0 A}\int_0^W \int_{-h}^0 (\{w\}\{\rho\} + \{w'\rho'\})dzdx \tag{2.9a}$$

where the first, $\{w\}\{\rho\}$, term is due to along-channel uniform changes in the average isopycnal slope. It affects *MKE* but not *EKE*. The second, $\{w'\rho'\}$, term involves changes in eddy kinetic energy associated with baroclinic instability. A second important conversion is that between mean and eddy kinetic energy:

$$C_{MKE\to EKE} = -\frac{1}{A}\int_0^w \int_{-h}^0 (\{u_x\}\{u'u'\} + \{v_x\}\{u'v'\} + \{u_z\}\{u'w'\} + \{v_z\}\{v'w'\})dzdx\ . \tag{2.9b}$$

The first two terms (involving u_x and v_x) represent barotropic instability, i.e., the energy transformation associated with mean horizontal velocity gradients. In practice, the v_x term, involving alongshore flow, dominates. The last two terms (which vanish if a quasigeostrophic approximation is made) are associated with unstable vertical shears, and are potentially important near fronts. Finally, the dissipation of eddy kinetic energy is given by

$$C_{EKE\to DISS} = \frac{1}{A}\int_0^W \int_{-h}^0 \left\{u'\left(D_V u'_z\right)_z + v'\left(D_V v'_z\right)_z\right\}dzdx \tag{2.9c}$$

In practice, this integral is dominated by contributions from the bottom boundary stress and the bottom boundary layer.

In order to assess the net importance of each conversion, time integrals of energy conversions were calculated up until the time t_M of maximum *EKE*. Specifically, C^{ρ} is the integral of the $\{w'\rho'\}$, baroclinic instability, portion of (2.9a), C^{x} is the integral of the $\{v_x\}\{u'v'\}$, barotropic instability, portion of (2.9b) and C^{z} is the integral of the $\{v_z\}\{v'w'\}$, shear instability, portion of (2.9c). The maximum value of *EKE* is denoted in Table 1 as EKE_M. These values are tabulated in Table 1.

A representative alongshore wavelength λ is estimated at $x = (x_F + \Delta x)$, the offshore edge of the initial front, and recorded in Table 1 for the time of maximum *EKE*, $t = t_M$. At this frontal location, the alongshore autocovariance function of u is calculated at several depths, and similar calculations are done both 2 km farther offshore and closer inshore. All of these are depth-weighted and then used to create a single averaged covariance function. The first zero crossing of this covariance function is taken to be the be approximately one quarter of a typical wavelength λ. This is a very reasonable approximation for narrow-band (in wavelength) processes.

3. Results

3.1. Representative evolutions

Not surprisingly, when there is no wind stress, *APE* remains constant (Fig. 2, upper panel) until perturbations reach a substantial amplitude and *EKE* begins to grow rapidly (Fig. 2, middle panel). In contrast, when there are upwelling favorable winds, the cross-shelf circulation flattens out isotherms initially (Fig. 1b), and this is expressed as a decrease in *APE* (Fig. 2, upper panel). *APE* then recovers partially and remains nearly constant until, again, *EKE* reaches a substantial amplitude (Fig. 2, middle panel). In contrast, downwelling favorable winds steepen the temperature front (Fig. 1c), hence increase *APE* (Fig. 2, top panel). Again, *APE* declines as *EKE* (Fig. 2, middle) grows. In all cases, *EKE* peaks after a few tens of days, and *APE* decreases nearly monotonically with time after *EKE* reaches finite amplitude (Fig. 2, top two panels). In downwelling cases, there is typically a brief period (t = 3–10 days for run 8) early in the model run where near-surface (e.g., Thomas and Taylor 2010) and near-bottom (e.g., Allen and Newberger, 1998) slanted in (x, z) roll structures having wavelengths of O(1 km) develop. These are especially apparent in cross-shelf velocity where the amplitudes are about 0.05 m/s. These features are taken to represent the results of symmetric instability, and they are quickly eliminated at the front and inshore as three-dimensional instabilities grow. At later times, weak (about 0.01 m/s in u) cells in the bottom boundary layer still exist offshore of the front. In contrast to many instability problems (e.g., Brink, 2016) where the representative alongshore wavelength λ tends to increase with *EKE*, there are at most weak temporal trends of this sort in the present context (Fig. 2, lowest panel). Note that the length scale estimates for times earlier than about 25 days in the upwelling ($\tau_A > 0$) case should not be taken too seriously because for earlier times, *eke* levels are very low and disturbances then are confined within about 10 km of the coast.

At the time of maximum *EKE* (Fig. 3), *eke* is largest at the surface and near the initial offshore location of the front, again consistent with Zhang and Gawarkiewicz (2015), but somewhat surprisingly because the wind affects the frontal location well before *EKE* approaches a maximum. Also, as expected when baroclinic instability is dominant, the mean isotherms are all flattened relative to conditions before substantial instability (compare Fig. 1 with Fig. 3).

Time series of the energy conversions (Fig. 4) demonstrate that the

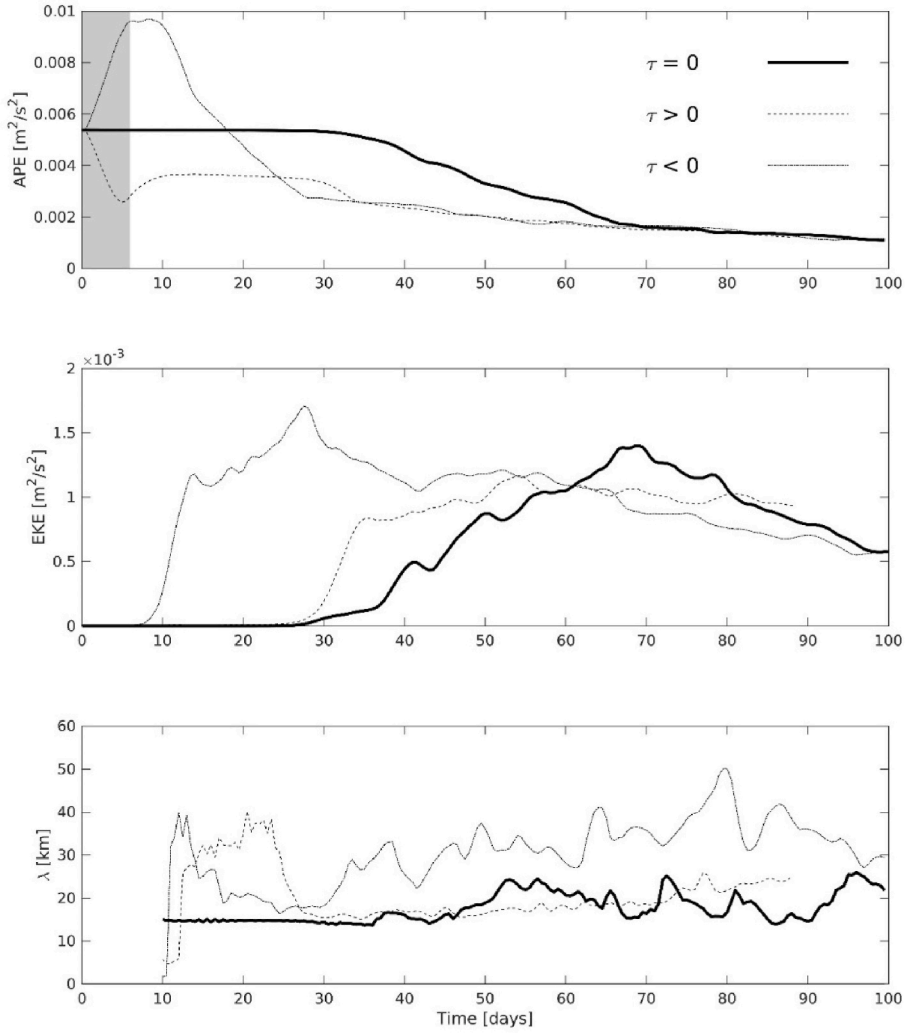

Fig. 2. Time series of *APE* (upper panel), *EKE* (middle panel) and representative alongshore wavelength (lower panel) for runs with no alongshore wind stress (run 6), upwelling-favorable wind stress (run 8, $\tau > 0$) and with downwelling favorable wind stress (run 3, $\tau < 0$). These are the same runs as in Fig. 1. The shaded area in the first panel represents the period during which the alongshore wind stress is non-zero. Length scales are evaluated at $x = (x_F + \Delta x)$.

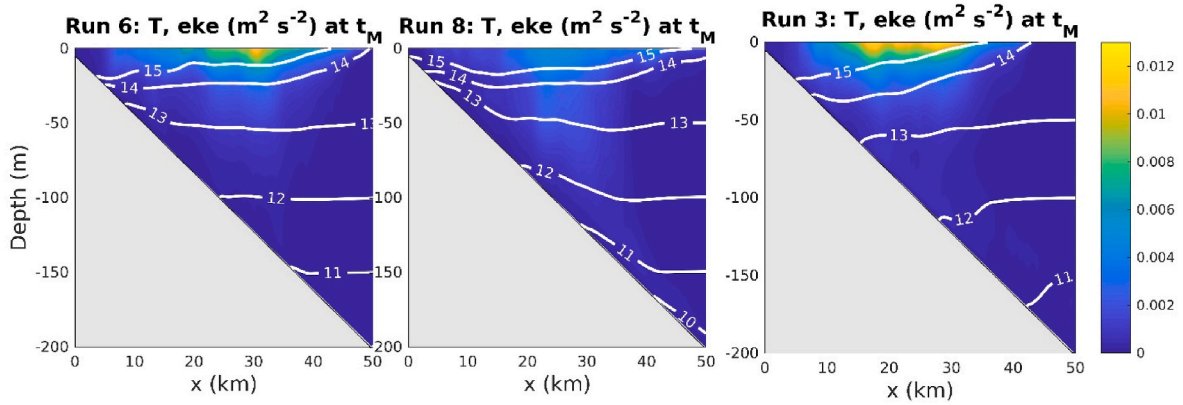

Fig. 3. Eddy kinetic energy, *eke* (colors) and along-channel averaged temperature (white contours) at $t = t_M$, the time of maximum *EKE,* for runs with no alongshore wind stress (run 6, $\tau_A = 0$), upwelling-favorable wind stress (run 8, $\tau_A > 0$) and with downwelling-favorable wind stress (run 3, $\tau_A < 0$). These are the same runs as in Figs. 1 and 2. The contour interval for temperature is 1 °C. The *eke* maxima occur at the surface 30, 26 and 28 km from shore when t_M = 69, 54 and 28 days, respectively for the three panels.

most important terms, in all three runs, are those representing baroclinic instability (Eqn. (2.9a): solid curves) and dissipation (Eqn. (2.9c): dash-dot curves). For each case, the vertical shear instability (the $\{\nu_z\}$ term in eqn. (2.9b): dotted curve) makes a modest contribution to the growing instability. The barotropic instability term in (2.9b) typically has an instantaneous magnitude (not shown) similar to the other conversions,

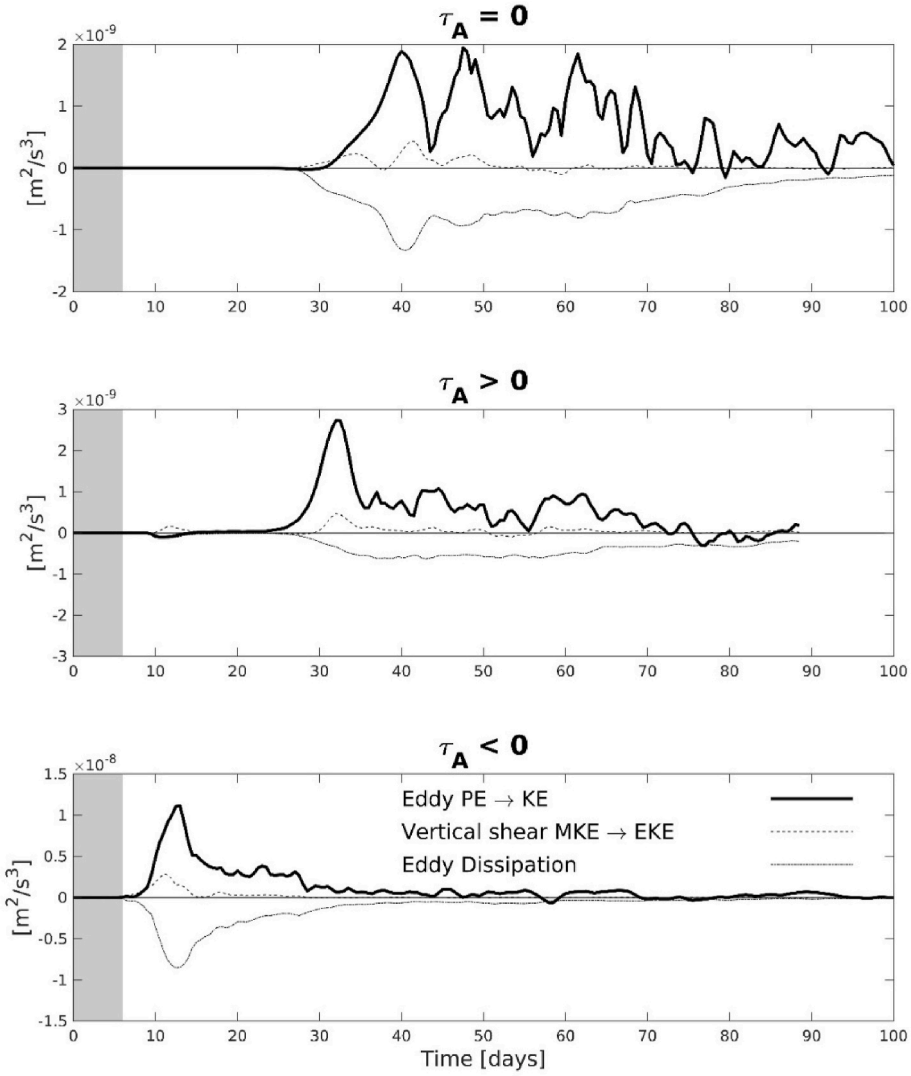

Fig. 4. Time series of energy conversions for runs with no alongshore wind stress (run 6, $\tau_A = 0$: upper panel), upwelling-favorable wind stress (run 8, $\tau_A > 0$: central panel) and with downwelling favorable wind stress (run 3, $\tau_A < 0$: lower panel). These are the same runs as in Figs. 1–3. The shaded area represents the time during which the wind stress is nonzero. The "vertical shear" conversion is associated with $\{\nu_z\}$ in (2.9b). Note that the vertical scale varies from panel to panel.

but it varies substantially temporally in sign such that it usually makes little net integrated contribution (Table 1).

These findings are very representative of the other runs carried out as part of this study. In no model run does the eddy growth eliminate the initial front, although it becomes very contorted by the eddy field, and, in the upwelling case, it becomes somewhat more diffuse. Specifically, in Fig. 5, the case with downwelling (run 3) consistently shows a very sharp transition from red to blue, a 2° jump, but with upwelling (run 8), the frontal boundary is clearly more gradual (i.e., there are more intermediate colors, such as light blue or yellow, present).

Invariably, over all the runs reported here, the time history of *APE* follows one of the three patterns represented in Fig. 6. When there is no wind stress, *APE* remains effectively constant at its initial value until the growing instabilities begin to erode the *APE* pool. In this case, a good measure of the *APE* available for a growing instability is the initial value, APE_0. When there is an upwelling favorable wind stress, *APE* is initially reduced and then rebounds to a nearly constant level until eddies reach finite amplitude. The rebound is associated with wind-driven alongshore flow driving a short-lived upslope dense water transport in the bottom boundary layer. In this case, the *APE* available for eddy growth is represented by the relatively constant plateau value, APE_P. Finally, when there is a downwelling-favorable wind stress, the front steepens and *APE* increases to a temporal maximum, APE_M, and then decreases as *EKE* reaches finite amplitude. This diversity of trajectories motivates the definition of a single *APE* value, the "relevant *APE*", APE_R, which is simply APE_0 when $\tau_A = 0$, APE_P when $\tau_A > 0$ and APE_M when $\tau_A < 0$.

3.2. General trends

Invariably, *EKE* never reaches appreciable values until after the wind stress ceases (e.g., Fig. 2). The model results, in all but 2 out of 44 cases, show that the baroclinic instability process dominates *EKE* growth (Table 1: C^ρ, C^x, C^z). Specifically, the baroclinic conversion C^ρ is usually the largest, often by an order of magnitude. The two cases, 13 and 14, where this is not true are dominated by barotropic instability C^x, and are excluded from all further considerations. Both of these runs have a smaller f (0.5×10^{-4} 1/s) and thus have stronger shears for a given frontal thermal structure compared with examples where f is larger. Thus, it seems likely that barotropic instability (which leads to larger spatial scales: see λ for runs 12–14 compared to runs 3–8) will be relatively more effective at low latitudes than baroclinic instability. In 25 out of the remaining 42 cases, vertical shear instability C^z is the second largest contributor, while second place is taken by barotropic instability in 17 cases. Barotropic instability's role is rather inconsistent, however,

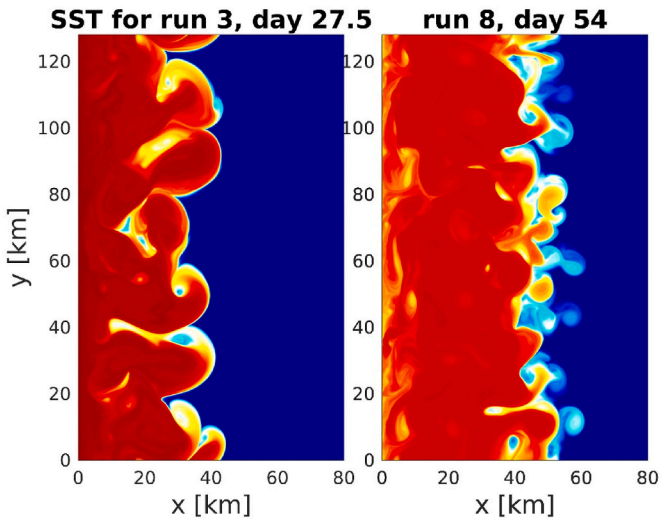

Fig. 5. Sea surface temperature at the time of maximum Eddy Kinetic Energy for runs 3 (downwelling favorable winds, $\tau_A < 0$: left panel) and 8 (upwelling favorable winds, $\tau_A > 0$: right panel). The two runs are identical except for the sign of the wind forcing. The temperature ranges from 14° (dark red) to 16° (deep blue).

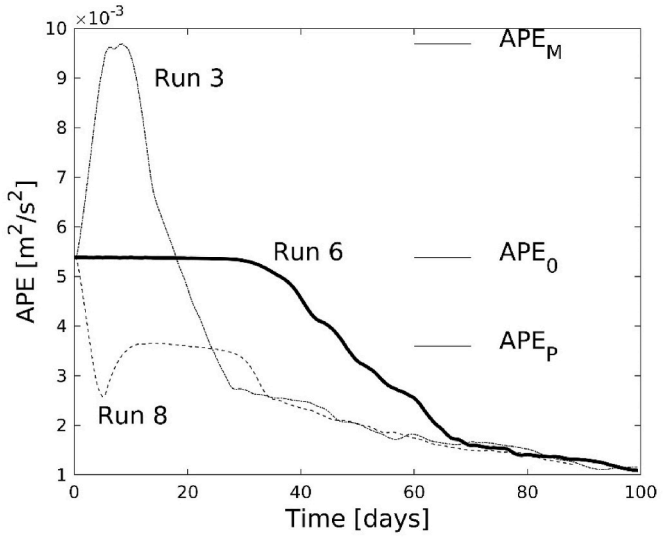

Fig. 6. Time series of *APE* for runs 3, 6 and 8 (reproducing the plots of Fig. 2a) giving definitions of initial *APE* (APE_0: relevant for runs where there is no wind stress to modify *APE*), maximum *APE* (APE_M: relevant for runs with downwelling-favorable, $\tau_A < 0$, wind stress), and the *APE* plateau (APE_P: relevant for runs where upwelling-favorable winds, $\tau_A > 0$, decrease *APE*).

because it represents a net sink of *EKE* ($C^x < 0$) in 14 of the 42 cases. The vertical shear conversion is only an *EKE* sink in 3 cases. All considered, for the collection of runs presented here, it is reasonable to say that baroclinic instability is the dominant mechanism.

There is a vague tendency for EKE_M (i.e., the time maximum of *EKE*) to decrease as τ_A increases from negative to positive values (i.e., from downwelling to upwelling: Fig. 7, upper panel), and it appears that doubling the application time for the wind stress with constant τ_A is equivalent to doubling the wind stress (runs 8 vs. 43 in Table 1). The relevant *APE* (Fig. 7, lower panel), on the other hand, shows a more pronounced, but still not completely consistent, tendency to decrease with increasing τ_A, consistent with upwelling flattening temperature surfaces and downwelling steepening them (Fig. 1). The two run sequences where relevant *APE* increases for positive τ_A (runs 1–8 and 34–36) both appear to represent cases where upwelling removes the initial buoyancy current's water offshore, and deeper, upwelled water approaches the surface near the coast (e.g., Fig. 3, middle panel and Fig. 5, right panel).

In some cases, the dependence of EKE_M on parameters is relatively clearcut. For example, EKE_M increases as the frontal thickness Δx, temperature contrast ΔT or slope γ increases (Fig. 8a, c, 8d). The dependencies on ΔT and on γ seem especially intuitive because they reflect directly on the strength of the front and its current shear. Further, the instability is more energetic as the front's distance from the coast x_F increases (Fig. 8b), a finding consistent with Hetland (2017). This dependence on x_F is rationalized by the scalings in section 4.2.1, which show that the pool of *APE* increases with the front's distance from the coast.

In other cases, the parameter dependence is less straightforward. For example (Fig. 9a), smaller f leads to stronger instabilities when $\tau_A = 0$ (dropped run 13 vs. 6), but the opposite occurs when $\tau_A > 0$ (dropped run 14 vs. 8). Further, when $\tau_A < 0$ (run 12 vs. 3), EKE_M remains essentially unchanged when f changes. The $\tau_A = 0$ result is understandable in light of the thermal wind relation: smaller f leads to larger shears, hence a stronger role for barotropic instability. However the results with $\tau_A \neq 0$ apparently reflect the further role f plays beyond determining the shear across a given front. For example, the cross-shelf Ekman transport and the depth over which it occurs (hence the Ekman velocity: transport divided by depth) both depend on f, and these in turn determine the degree to which winds reshape the front (Section 4), hence its *APE*.

When $\tau_A \leq 0$, EKE_M increases as the bottom slope α increases (Fig. 9b), but it decreases when $\tau_A > 0$. This finding for $\tau_A \leq 0$ is perhaps unexpected, given the quasigeostrophic linear stability growth rates of Blumsack and Gierasch (1972) which suggests weaker instability for larger bottom slopes. Of course, finite amplitude parameter dependencies do not need to agree with linearized solutions, nor do quasigeostrophic (weak frontal slope) findings obviously carry over either. Indeed, scalings (e.g., Section 4.2, below) rationalize the $\tau_A \leq 0$ result because a steeper bottom implies a greater *APE*. EKE_M is not overly sensitive to variations in ambient stratification Γ (Fig. 9c) or in bottom frictional coefficient r (Fig. 9d), and what dependencies there are sometimes are nonmonotonic and inconsistent among wind cases. The absence of a strong frictional dependence is somewhat startling, given the clear importance of dissipation in the *EKE* evolution (Fig. 4). On the other hand, a weak frictional dependence would seem consistent with both the *eke* distribution (Fig. 3) and Empirical Orthogonal Function calculations executed near the *eke* maximum [i.e., at $x = (x_F + \Delta x)$: not shown]: both of these measures show that velocity fluctuations (hence, likely, stress fluctuations) are very weak near the bottom. These calculations show that, at least for the present parameter range, the degree of eddy surface-intensification does not depend noticeably on bottom friction. This contrasts with models of eddies driven by surface cooling over the shelf, where the degree of surface intensification clearly depends on bottom friction (e.g., Pringle, 2001; Brink, 2017), especially when r is small. The role of bottom friction is discussed further in section 5, below.

4. Scalings

4.1. Introduction

At this point, it is useful to encapsulate the model results in terms of scalings. These serve more than one function. Primarily, the scalings represent convenient formulae that can potentially be applied to real-world conditions and so predict the scales or degree of instability. If these predictions compare well to observations, it bodes well for the applicability of the model results. If the scalings do not serve well vs. observations, information may be gained about what is missing from the current formulation. Further, in some cases, the argument leading up to

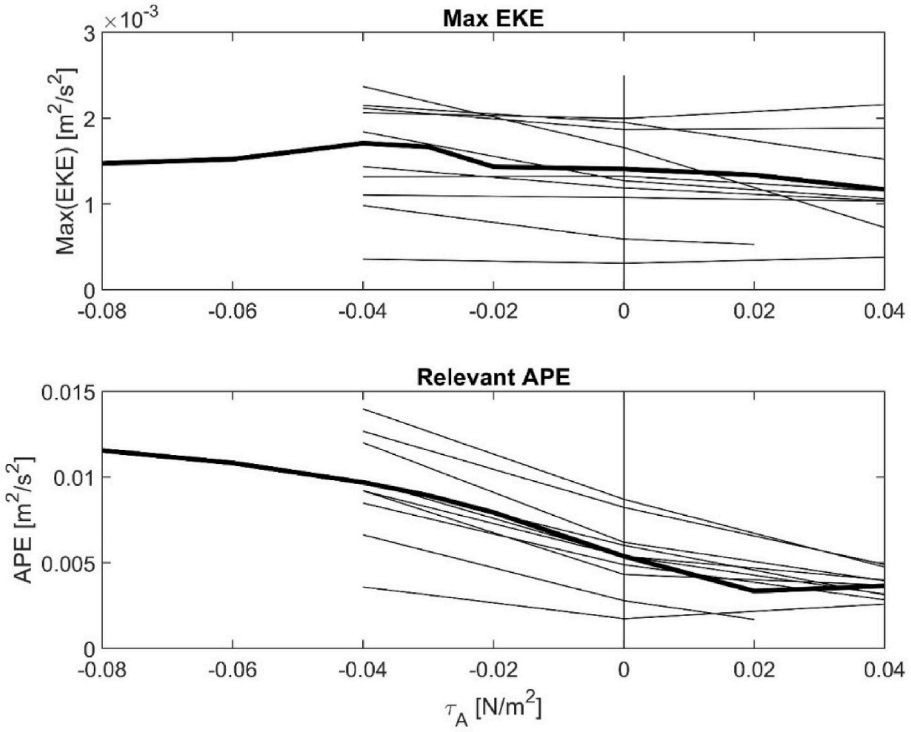

Fig. 7. Maximum spatially averaged *EKE* (i.e., EKE_M) as a function of wind stress amplitude τ_A (upper panel) and relevant *APE* (i.e., APE_R) as a function of wind stress amplitude τ_A (lower panel). Each line represents a set of runs that are identical except for the wind stress amplitude. In both panels, the heaviest line represents the grouping of runs 1–8.

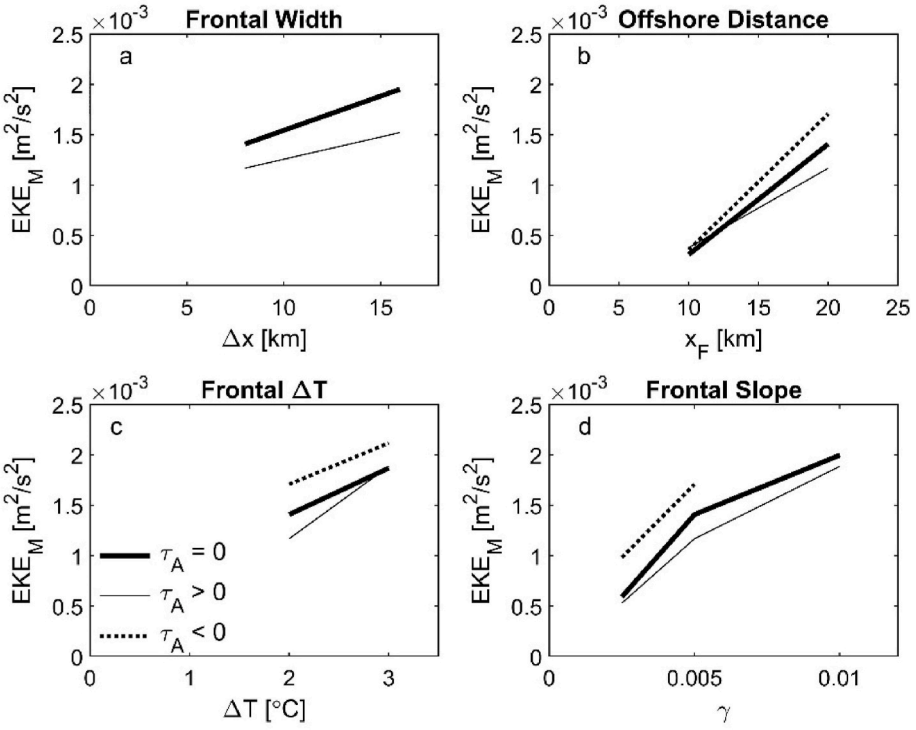

Fig. 8. Sensitivity of time-maximum *EKE* to model parameters. a) frontal width Δx (runs 6, 8, 3, 32, 33, 31), b) distance of the front from the coast x_0 (runs 6, 8, 3, 35, 36, 34), c) temperature contrast across the front ΔT (runs 6, 8, 3, 10, 11, 9), d) frontal slope γ (runs 6, 8, 3, 16, 17, 15, 19, 20).

a scaling can provide some insight into the underlying dynamics.

One might expect that the eddy kinetic energy (represented by EKE_M) of a baroclinically unstable system would be well correlated with the available potential energy (represented by APE_R). Indeed, this is the case: the correlation is 0.87, 0.89 and 0.72 for $\tau_A = 0$ (12 runs), >0 (14 runs) and <0 (16 runs), respectively. Thus, it is reasonable to

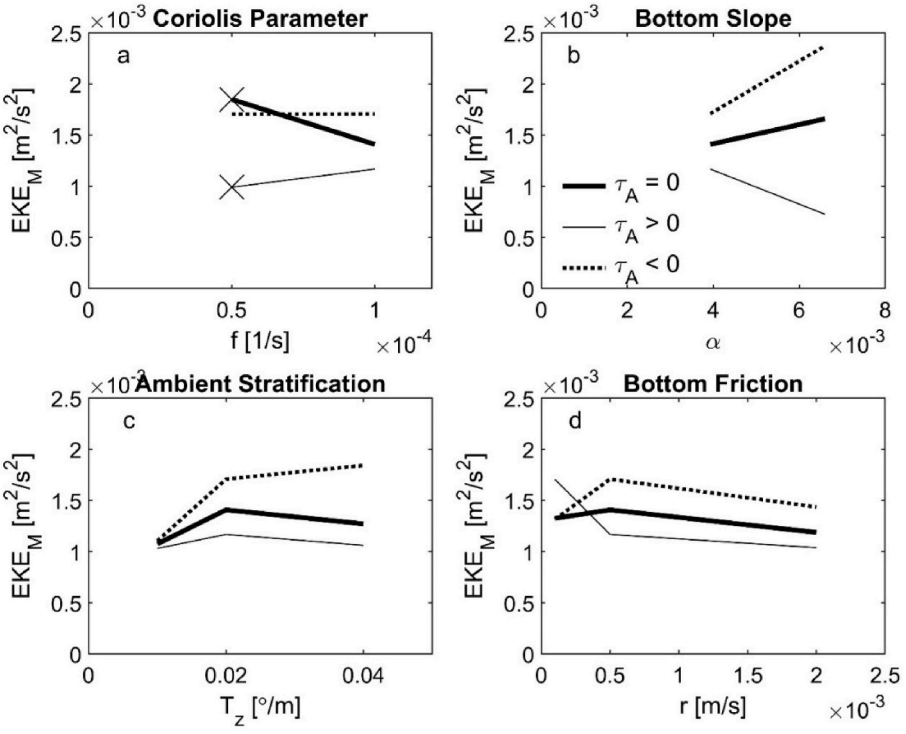

Fig. 9. Sensitivity of time-maximum *EKE* to model parameters. a) Coriolis parameter f (runs 6, 8, 3, 13, 14, 12), (The "x" symbol denotes runs where baroclinic instability was not dominant.) b) Bottom slope α (runs 6, 8, 3, 23, 24, 22), c) Ambient temperature stratification Γ (runs 26, 27, 25, 6, 8, 3, 29, 30, 28), d) Bottom frictional parameter r (38, 39, 37, 6, 8, 3, 41, 42, 40).

concentrate on APE_R as a starting point in developing a scaling for EKE_M. Further, one might expect that the efficiency of transfer from *PE* to *EKE* might depend, among other parameters, on bottom slope α, ambient stratification Γ, the Coriolis parameter f and/or bottom friction r. Some empirical exploration leads to the finding that an efficient estimate for EKE_M estimate is

$$< EKE_M >= \frac{a(1+cs)^n APE_R}{1+bR} \tag{4.1a}$$

where the angle brackets represent a scaling approximation and

$$R = \frac{r}{fH}, H = h_0 + \alpha(x_F + \Delta x) \tag{4.1b, c}$$

and the slope Burger number is

$$s = \frac{\alpha N}{f} = \frac{\alpha\sqrt{g\mu\Gamma}}{f} \tag{4.1.d}$$

(N being the buoyancy frequency). The coefficients in (4.1a) are found by minimizing the error of the fit so that $(a, n, c, b) = (0.086, 1, 8, 0)$, $(0.49, -1, 2, 0)$, $(0.11, 1, 2, 0.2)$ for $\tau_A = 0$, >0 and < 0, respectively. The correlations of the fits are (0.95, 0.89, 0.83). Frictional corrections $(b \neq 0)$ yield only minor (a few %) improvements to the fit for $\tau_A \geq 0$, and are thus neglected under those conditions. The stated values of n, c and b yield fits that are (40, 4, 26)% better than would be the case with c and $b = 0$. Presumably, the c correction reflects the efficiency with which *APE* can be converted to *EKE*. This s dependency is a good reminder that EKE_M depends on more than simply APE_R, and so the greater scatter in the EKE_M vs. τ_A plot (compared with the APE_R vs. τ_A plot: Fig. 7) is not unexpected.

4.2. Available potential energy

4.2.1. With no wind stress

APE_R is easiest to estimate for the case with $\tau_A = 0$, since it is simply the initial *APE* which only involves an unperturbed front (Fig. 10). The approach is to estimate the potential energy anomaly inshore of $x = W$ that is associated with the front (i.e., how different is the *PE* per unit mass inshore of the front relative to offshore?). For a domain infinite in x, if all isotherms are adiabatically flattened, the waters inshore of the front are stretched out near the surface to be an infinitesimally thin layer at the surface ($z = 0$) and thus not contributing to the adjusted *PE*. Thus, the initial *PE* anomaly (relative to flat isopycnals), averaged over the total mass inshore of W becomes APE_0. Because the background thermal stratification Γ is uniform everywhere, it creates no anomaly and so is

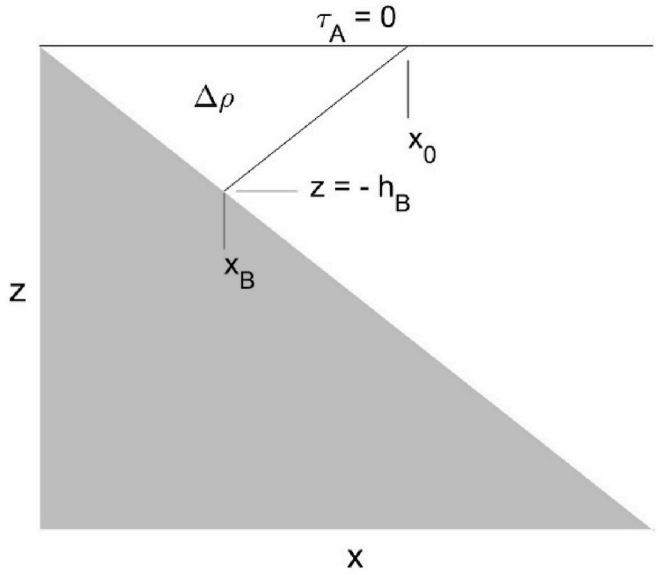

Fig. 10. Schematic used in estimating APE_R (=APE_0) when no wind stress has been applied.

irrelevant to this calculation. For simplicity, the continuous horizontal temperature variation described by (2.3) is collapsed to a sharp interface (located at the center of the actual front) which intersects the surface at $x_0 = x_F + \Delta x/2$. Given that the interfacial slope is γ, the location where the front encounters the bottom is

$$x_B = \frac{\gamma}{\alpha+\gamma} x_0 \tag{4.2a}$$

and the depth there (neglecting h_0 henceforth) is

$$h_B = \alpha x_B \, . \tag{4.2b}$$

The cross-sectional area inshore of the front is

$$A_F = \frac{1}{2} h_B x_0 \tag{4.2c}$$

and the average *pe* anomaly (relative to $z = 0$) for the triangular area inshore of the front is

$$-g\Delta\rho h_B \ / 3 \tag{4.3}$$

with

$$\Delta\rho = -\rho_0 \mu \Delta T$$

Thus, the *PE* anomaly per unit mass inshore of $x = W$ is

$$< APE_0 > \ = -\frac{g\Delta\rho h_B A_F}{3\rho_0 A_W} = \frac{g\mu\Delta T(\alpha\gamma x_0)^2}{6(\alpha+\gamma)^2 A_W} \tag{4.4a}$$

and the area inshore of $x = W$ is

$$A_W = \frac{1}{2}\alpha W^2 \, . \tag{4.4b}$$

For the 12 runs with no wind forcing, the scaling (4.4a) is related to the actual APE_0 as

$$APE_0 = \eta_0 < APE_0 > \tag{4.5}$$

where $\eta_0 = 0.42$ and the correlation of the fit is 0.92.

4.2.2. With upwelling (positive) wind stress

When upwelling occurs, it is assumed that the front is distorted by surface Ekman transport in the manner described by Lentz (2004): (Fig. 11). In this case, the volume of water inshore of the front advected offshore has a *(x, z)* cross-sectional area (shown by shading in Fig. 11) of

$$A_F = \int_0^\infty \frac{\tau_0^y}{\rho_0 f} dt = U_E t_1 = \frac{\tau_A}{\rho_0 f} t_1 \tag{4.6}$$

Further, assume that there is slab-like flow in a surface boundary layer of thickness

$$\delta = \frac{Du*}{\sqrt{Nf}} \tag{4.7}$$

where D is taken to be 1.0 in the following: where u^* is the friction velocity. Thus, after the wind ceases, the offshore edge of the extrusion is at

$$x = x_1 = U_E t_1/\delta + x_0. \tag{4.8}$$

Meanwhile (neglecting changes to upper ocean density due to mixed layer deepening), the total volume of lighter water inshore of $x = x_1$ is conserved, so the inshore wedge (inshore of $x = x_2$) contracts as the extrusion grows. So, the area of the reduced nearshore wedge (denoted as unshaded upper-layer water in Fig. 11) is

$$A_A = \frac{1}{2}\alpha x_0^2 - U_E t_1 = \frac{1}{2}\alpha x_A x_2 \, . \tag{4.9}$$

Thus, the cross-sectional area of the extrusion is $(x_1 - x_2)\delta = U_E t_1$. Adding up the *PE* anomaly in the extrusion and in the wedge, the final *APE* per unit mass averaged over the area inshore of $x = W$ amounts to

$$< APE_P > \ = g\Delta\rho \left[\frac{1}{6}\alpha^2 x_A^3 + \frac{1}{2}\delta^2 (x_1 - x_2)\right] \Big/ (\rho_0 A_W) \, .$$

$$= g\Delta\rho \left[\frac{1}{6}\alpha^2 x_A^3 + \frac{1}{2}\frac{D^2 u_*^2}{Nf}(x_1 - x_2)\right] \Big/ (\rho_0 A_W) \tag{4.10}$$

The expression (4.10) is derived under the assumption that the offshore transport is not sufficient to cause the light water pool to separate entirely from the coast. Specifically, there is an assumption that

$$(t_1 + t_R) < t_S = \frac{A_F}{U_E} = \frac{\rho_0 x_0 h_B f}{2\tau_A} \tag{4.11}$$

where t_S is the approximate time to separation. It is also assumed that the extrusion does not carry too far offshore, i.e. that $x_1 < W$. This second assumption is readily addressed by adjusting the extruded area in (4.10). It should be noted that, in this parameter range, upwelling always leads to a decreased APE_R relative to the case with no winds because, overall, the isopycnals are flattened out.

Once the lighter inshore water has separated entirely from the coast, the *APE* evolves as in an upwelling front as described by Brink (2016), except that the wind application time is now roughly $(t_1\text{-}t_S)$ and that the cross-frontal density contrast is now roughly $(\Delta T + \Gamma h_f/2)$ where h_f is the water depth at the final location of the upwelling front at the inshore edge of the removed buoyant water (see Brink, 2016, but apply the time since surfacing rather than the time since wind onset). Of the present run collection, this fully upwelling situation occurs, and this correction applies, only for run 36, so there is little basis for evaluating its accuracy. With the added *APE* associated with the upwelling front, it becomes possible for APE_R to increase after upwelling (as indeed happens: for run 36 where APE_P is greater than the initial *APE*), in contrast to the situation where the buoyant waters do not separate from the coast.

For the 14 runs with positive wind forcing, the scaling for upwelling is related to the actual APE_P as

$$APE_P = \eta_P < APE_P > \tag{4.12}$$

where $\eta_P = 0.58$ and the correlation of the fit is 0.90.

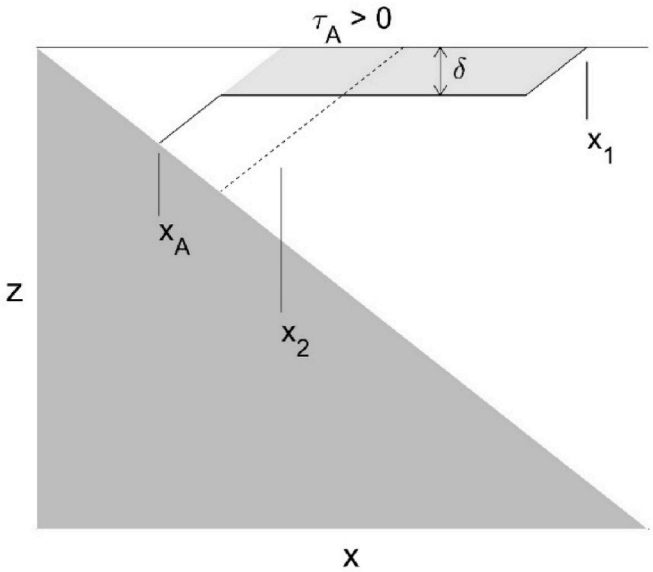

Fig. 11. Schematic used in estimating APE_R (=APE_P) after a positive wind stress has been applied. The dashed line indicates the original position of the front (as in Fig. 7), before the wind stress is applied.

4.2.3. With downwelling (negative) wind stress

If the time-integrated alongshore wind stress is not too strong, the APE_R is estimated by assuming that the effect of the onshore Ekman transport is simply to increase the frontal slope while keeping the volume of nearshore light water constant. Thus, the shaded area in Fig. 12a equals $U_E t_1$ and the areas of the two triangles in that figure have to match in order to conserve mass. Thus

$$-U_E t_1 = -z_P(x_0 - x_1)/2 \tag{4.13a}$$

and, conserving the volume inshore of the front,

$$x_1 = \sqrt{h_B x_0 \frac{\alpha + \gamma'}{\alpha\gamma'}} \tag{4.13b}$$

where h_B is the initial depth where the front intercepts the bottom (Fig. 10). Further, using

$$z_P = \gamma(x_P - x_0) = \gamma'(x_P - x_1), \tag{4.13c}$$

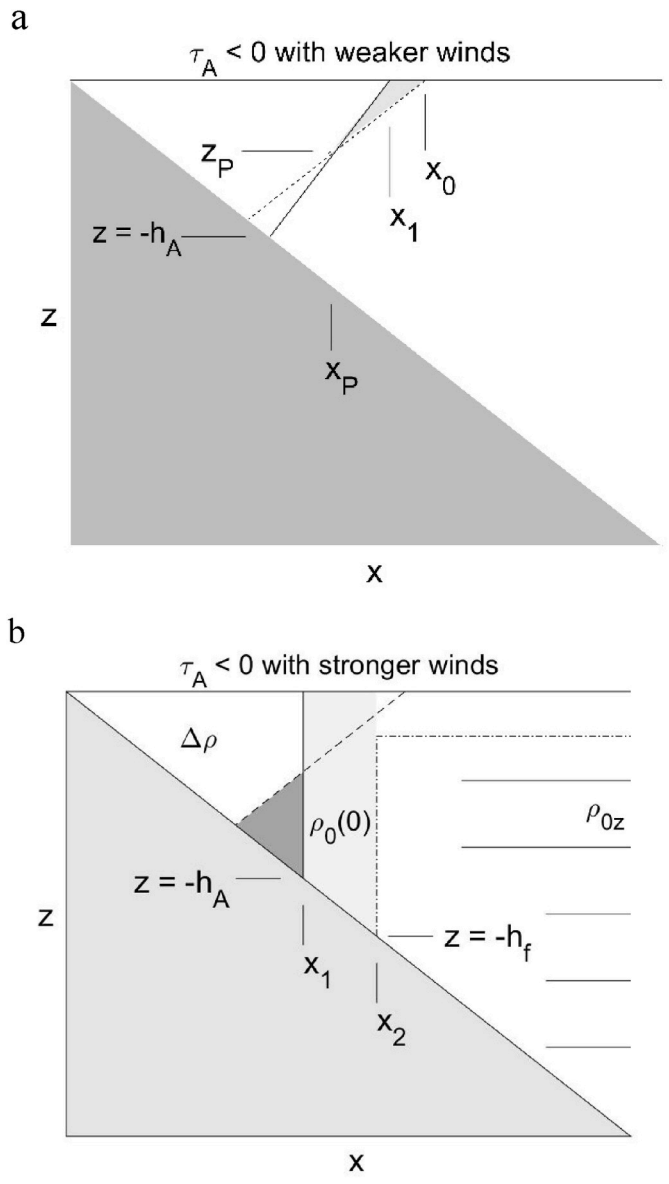

Fig. 12. Schematics used in estimating APE_R (=APE_M) after a downwelliing favorable wind stress has been applied. a) when winds are weak enough that the adjusted front is not vertical. b) when winds are strong enough that the front becomes vertical and continued downwelling occurs offshore of the front.

leads to

$$x_0 + \frac{z_P}{\gamma} = \frac{\gamma x_0 - \gamma' x_1}{\gamma - \gamma'} \tag{4.13d}$$

where γ' (which is calculated using 4.13a-d) is the front's slope after the wind ceases. The adjusted front intersects the bottom at $z = -h_A$ where

$$h_A = \frac{\alpha\gamma' x_1}{\alpha + \gamma'}\,. \tag{4.13e}$$

Thus, as in section 4.2.1, the average *ape* anomaly inshore of the front is

$$-g\Delta\rho h_A/3 \tag{4.14a}$$

and the estimated area-averaged *APE* is then

$$< APE_D > = -\frac{g\Delta\rho h_A A_F}{3\rho_0 A_W} = \frac{g\mu\Delta T(\alpha\gamma' x_1)^2}{6(\alpha + \gamma')^2 A_W}\,. \tag{4.14b}$$

This formulation is viable only up to the point where the front becomes vertical, i.e. so long as

$$U_E t_1 \le U_E t_V = \frac{\gamma}{2}\left(x_0 - \sqrt{\frac{h_B x_0}{\alpha}}\right)^2 \tag{4.15}$$

where t_V is the time it takes for the front to become vertical. The water depth at the adjusted frontal location is then $h_A = \alpha x_1$. Thus, at time $t = t_V$, when the front is vertical,

$$< APE_D > = \frac{g\mu\Delta T\alpha^2 x_0}{6(\alpha + \gamma)A_W}\,. \tag{4.16}$$

In all 16 model runs with downwelling favorable (negative) wind stress, t_V is exceeded.

After the front becomes vertical, it is assumed that near-surface waters downwell offshore of the initial (now vertical) front at $x = x_1$ into the region between x_1 and x_2 (the lightly shaded area in Fig. 12b). Thus, the temperature contrast between the homogeneous downwelled water (temperature T_2) and the ambient stratified water is proportional to Γh_f where h_f (= αx_2) is the depth at the outer front. The cross-sectional area of this downwelled water is then

$$U_E(t_1 - t_V) \cong \frac{1}{2}(x_2 - x_1)(h_f + h_A). \tag{4.17a}$$

It is then straightforward to estimate the *APE* per unit mass associated with the downwelled (lightly shaded) water by saying that the average *ape* in the downwelled region is

$$g\mu\Gamma(h_f + h_A)^2/2\,. \tag{4.17b}$$

All told, the *ape* associated with downwelling offshore of the front is added to that associated with the front having become vertical (eqn. (4.16): the dark shared area in Fig. 12b) to obtain a final estimate $<APE_M>$.

$$< APE_M > = < APE_D > + \frac{g\mu\Gamma(h_f + h_A)^2 U_E(t_1 - t_V)}{2A_W}\,. \tag{4.18}$$

For the 16 runs with negative wind forcing, this scaling for downwelling conditions is related to the actual APE_M as

$$APE_M = \eta_M < APE_M > \tag{4.19}$$

where $\eta_M = 0.66$ and the correlation of the fit is 0.92.

4.2.4. Applying the APE_R scalings

Comparing the APE_R scalings directly with EKE_M, the correlations are (0.95, 0.87, 0.81) for $\tau_A = 0$, >0 and < 0 respectively. This is to be compared with correlations of EKE_M with actual APE_R (section 4.1) of (0.87, 0.89, 0.72). Using the formulation (4.1a), but with the scalings for

APE_R yields empirical coefficients (a, n, c, b) = (0.61, 1, 3, 0), (0.17, −1, 2, 0), (0.063, 1, 4, 0) for the three wind ranges. The correlations associated with these fits are (0.98, 0.88, 0.91). In all cases, the s corrections reduce the error of the fit substantially, although the R corrections do not yield substantial improvements in any case. All told, the APE_R scalings appear to be rather successful, agreeing well with computed values and yielding fits for EKE_M that are substantially better than fitting with actual APE_R both when $\tau_A = 0$ and $\tau_A < 0$ (lower error by 44 and 28%), and comparable (about 2% worse) when $\tau_A > 0$. Why a scaling would appear to be more successful than the actual APE_R is not obvious.

The scalings are not perfect, of course. In particular, there are three cases (Fig. 7, upper panel, Table 1) where EKE_M increases with increasing positive τ_A (run sequences 10–11, 20–21 and 35–36, having larger ΔT, γ and smaller x_F, respectively relative to runs 1–8). In each case, the calculated EKE_M for the largest τ_A is larger than that for the next smallest τ_A, but the scalings predict a continued decrease in EKE_M with increasing τ_A. In the first and third instances, the failings are not large (7×10^{-5} m^2/s^2 or smaller) and so are probably near the noise level. The discrepancy is more pronounced (3×10^{-4} m^2/s^2) for runs 20–21 and occurs even though APE declines with τ_A. It thus appears that, while the scalings for EKE_M are successful in most cases, they are less successful with a strongly sloping initial front.

4.3. Alongshore wavelength

There are a number of possibilities for scaling the alongshore wavelength at the time of maximum EKE. These include an internal Rossby radius based on the interior stratification

$$\lambda_{RR} = \frac{NH}{f}, \tag{4.20a}$$

a Rossby radius based on the frontal density difference

$$\lambda_F = \frac{\sqrt{g\,\mu \Delta T H}}{f}, \tag{4.20b}$$

an inertial length scale

$$\lambda_I = \frac{\sqrt{EKE_M}}{f}, \tag{4.20c}$$

and a topographic Rhines (1977) scale

$$\lambda_{Rh} = \sqrt{\frac{\sqrt{EKE_M}}{\beta_T}} \tag{4.20d}$$

where β_T is a topographic beta

$$\beta_T = \frac{f\alpha}{H}. \tag{4.20e}$$

Simply correlating these scales with the wavelength λ estimated from the models (Table 1) yields, for each of (4.20 a-d), correlations of 0.73 or better when $\tau_A < 0$. However, when $\tau_A \geq 0$, clearly the best correlation (0.68 for $\tau_A > 0$ and 0.88 for $\tau_A = 0$) occurs with λ_{RR} (4.20a). Because the Rossby radius scaling is the only one that works tolerably well for all three wind cases, it is used in the following.

A somewhat better parametrization is found empirically to be

$$< \lambda > = \frac{m}{1 + ds}\frac{NH}{f}, \tag{4.21}$$

where (m, d) = (4.9, 2), (4.6, 3), (4.0, 1) for τ_A = 0, >0 and < 0, respectively. The improvement in the fit obtained by allowing $d \neq 0$ is rather modest, however: 11–16% error reduction, depending on the case. For comparison, Zhang and Gawarkiewicz (2015), treating only cases with $\tau_A = 0$, use the same functional form (4.21) (although they define s somewhat differently) and obtain $d = 2.7$.

An interesting aspect of the scaling (4.21) is that the result depends only on the initial conditions, and is independent of the properties of the eddy field. This contrasts with other types of instability over the shelf (e.g., with wind driving in the absence of an initial buoyancy current front: Brink, 2016) where the alongshore length scale of the eddy field is related to the Eddy Kinetic Energy (as is the cases for scales 4.20c, d). This point is addressed in the following section.

5. Discussion and conclusions

The central physical mechanism treated here is relatively straightforward. An upwelling-favorable wind stress leads to offshore Ekman transport and a general flattening of the frontal isopycnals. This flattening translates into a decrease in the APE that in turn leads to decreased EKE. If the winds are applied long enough, however, a new, additional upwelling front forms inshore of the exported buoyant water (as discussed in conjunction with eqn. (4.11)), and the APE (hence EKE) can ultimately increase with τ_A. On the other hand, a downwelling favorable wind stress tends to make the frontal density surfaces more nearly vertical, thus increasing the APE. Once the initial front becomes vertical, a new downwelling front develops just offshore (as sketched in Fig. 12), continuing the APE increase. Thus one might expect EKE to increase in the presence of downwelling-favorable winds, as generally occurs (Fig. 7). Although the model runs are long compared with, say, individual wind events, at least some effects of winds on frontal instability become obvious within 10–20 days (Fig. 4), so it is not unreasonable believe that the present results are relevant to real oceanic conditions. As suggested by Fig. 7, the relation between APE and EKE is hardly ironclad. Indeed, the success of (4.1) demonstrates that this is not a one-to-one relationship: other factors (such as bottom slope or Coriolis parameter) affect the efficiency with which eddies are generated for a given APE arrangement.

One peculiarity of the EKE_M scalings is the absence of any dependence on bottom friction (section 4.2.4), even though near-bottom dissipation clearly plays a major role in the evolution of the eddy field (Fig. 4). It seems likely that this apparent inconsistency can be accounted for as follows. During eddy evolution, bottom friction acts, through a stratified spindown process, to eliminate eke at depth. This would occur over a vertical scale (St. Maurice and Veronis, 1975) of $L^z = f/(Nk)$ (where $k = \lambda/(2\pi)$ is a horizontal wavenumber and λ the alongshore wavelength) and over a time scale of $T^f = f/(kNr)$. For the present selection of runs, L^z is 35–86 m (always less than the water depth at $x = x_F + \Delta x$) and T^f = 0.3–8 days. This decay time scale is short enough that eddy energy at depth will be largely destroyed during the roughly 20–150 day time t_M it takes for EKE to reach its maximum value. That is to say that there is plenty of time for frictional dissipation to assure a surface-intensified eddy field. The surviving eddy field, being out of contact with the bottom, is not subject to spindown. Thus, while bottom friction is presumably important for creating the observed eddy field structure, it does not govern the amplitude of the remaining eddies so long as dissipation is strong enough to spin down the deeper waters before $t = t_M$.

An intriguing aspect of these calculations is the confirmation that the typical alongshore length scale of the resulting eddies is closely related to a simple internal Rossby radius of deformation (4.20a, 4.21), a result previously stated by Zhang and Gawarkiewicz (2015). Other studies of evolved eddies over the shelf find that the length scale at the time of maximum EKE is strongly affected by the eddy amplitude, e.g., an inertial scale (4.20c: Brink 2016) or a topographic Rhines scale (4.20d: Brink, 2017). The present result appears to be consistent with the water column's overall stratification at the location of the initial front's surface intersection (which is the approximate location of the spatial maximum EKE) being only modestly modified by the surface-intensified eddy field. The applicability of λ_{RR} is presumably associated with the Rossby radius at the front (the scale expected for initial, linearized baroclinic instability) being larger than the Rhines scale λ_{Rh} at any time. Indeed, λ_{RR} exceeds λ_{Rh} for every model run carried out, typically by a factor of

about 2 or more. This scale discrepancy then suggests that there should be no tendency for the eddy field to evolve to larger scales.

Most of the model runs in Table 1 derive their *EKE* from energy exchanges dominated by baroclinic instability. The two cases (13 and 14) where this is not true are dominated by barotropic instability and involve an unusually small Coriolis parameter. For the range of parameters used here, both shear and barotropic instabilities can be secondary contributors or they can act to increase *MKE*. While the vertical shear mechanism almost always contributes to eddy growth, the lateral shear mechanism (barotropic instability) is less consistent in sign. Inspection of Table 1 does not lead to any obvious pattern as to the sense of these contributions. Nor is it obvious how seriously we should take these secondary terms. There is clearly more that could be done on these eddy processes that lead to the offshore mixing of buoyancy currents.

At this point, it is desirable to compare the present results to existing observations or model simulations. However, there do not appear to be any observational studies that relate changes in Eddy Kinetic Energy in a buoyancy current to wind stresses (although Weingartner et al., 1999, do give an example of a baroclinically unstable buoyancy current without considering winds). This absence of observational evidence is perhaps not surprising because of the many factors that affect buoyancy current structure and variability. Amongst simulation numerical models, the situation is similar. One very interesting comparison, however, is provided by Magaldi et al. (2010) who treat the Western Adriatic Current with realistic topography but idealized winds. Their qualitative result is the opposite to the present findings: downwelling leads to weaker eddy variability than does upwelling. Some caution is required, however, because their relevant model runs are relatively short (15 days) and because their irregular topography can potentially generate coastal-trapped lee waves (e.g., Zhang and Lentz, 2017), hence enhanced alongshore variability, during upwelling but not during downwelling. At this point, it is difficult to evaluate the alternative possibilities. Clearly, there is scope for more investigations.

Declaration of competing interest

There is no conflict of interest, financial or otherwise, that I can perceive about this submission.

Acknowledgements:

Thoughtful comments from Gordon Zhang and an anonymous reviewer greatly improved this submission.

References

Allen, J.S., Newberger, P.A., 1998. On symmetric instabilities in oceanic bottom boundary layers. J. Phys. Oceanogr. 28, 1131–1151.
Blumsack, S.L., Gierasch, P.J., 1972. Mars: the effects of topography on baroclinic instability. J. Atmos. Sci. 29, 1081–1089.
Brink, K.H., 2016. Continental shelf baroclinic instability. Part I: relaxation from upwelling or downwelling. J. Phys. Oceanogr. 46, 551–568.
Brink, K.H., 2017. Surface cooling, winds and eddies over the continental shelf. J. Phys. Oceanogr. 47, 879–894.
Chapman, D.C., Lentz, S.J., 1994. Trapping of a coastal density front by the bottom boundary layer. J. Phys. Oceanogr. 24, 1464–1479.
Chen, S.-N., Chen, C.-J., Lerczak, J.A., 2019. On baroclinic instability over continental shelves: testing the utility of Eady-type models. J. Phys. Oceanogr. 50, 3–33.
Flagg, C.N., Beardsley, R.C., 1978. On the stability of the shelf water/slope water front south of New England. J. Geophys. Res. 83, 4623–4631.
Fong, D.A., Geyer, W.R., Signell, R.P., 1997. The wind-forced response on a buoyant coastal current: observations of the western Gulf of Maine. J. Mar. Syst. 12, 69–81.
Griffths, R.W., Linden, P.F., 1981. The stability of buoyancy-driven coastal currents. Dynam. Atmos. Oceans 5, 281–306.
Haidvogel, D.B., Arango, H.G., Hedstrom, K., Beckmann, A., Malanotte-Rizzoli, P., Shchepetkin, A.F., 2000. Model evaluation experiments in the North Atlantic basin: simulations in nonlinear terrain-following coordinates. Dynam. Atmos. Oceans 32 (239), 281. https://doi.org/10.1016/S0377-0265(00)00049-X.
Hetland, R.D., 2017. Suppression of baroclinic instabilities in buoyancy-driven flow over sloping bathymetry. J. Phys. Oceanogr. 47, 49–68.
Hickey, B.M., Pietrafesa, L.J., Jay, D.A., Boicourt, W.C., 1998. The Columbia River plume study: subtidal variability in the velocity and salinity fields. J. Geophys. Res. 103, 10,339-10,368.
Lentz, S.J., 2004. The response of buoyant coastal plumes to upwelling-favorable winds. J. Phys. Oceanogr. 34, 2458–2469.
Lentz, S.J., Largier, J., 2006. The influence of wind forcing on the Chesapeake Bay buoyant coastal current. J. Phys. Oceanogr. 36, 1305–1316.
Magaldi, M.G., Özgökmen, T.M., Griffa, A., Rixen, M., 2010. On the response of a turbulent coastal buoyant current to wind events: the case of the Western Adriatic Current. Ocean Dynam. 60, 93–122.
Moffat, C., Lentz, S., 2012. On the response of a buoyant plume to downwelling-favorable wind stress. J. Phys. Oceanogr. 42, 1083–1098.
Pringle, J.M., 2001. Cross-shelf eddy heat transport in a wind-free coastal ocean undergoing winter time cooling. J. Geophys. Res. 106, 2589–2604.
Rhines, P.B., 1977. The dynamics of unsteady currents. In: Goldberg, E.D., McCave, I.N., O'Brien, J.J., Steele, J.H. (Eds.), The Sea, ume 6. J.H. Wiley, pp. 189–318.
Rogers-Cotrone, J., Yankovsky, A.E., Weingartner, T.J., 2008. The impact of spatial wind variations on freshwater transport by the Alaska Coastal Current. J. Mar. Res. 66, 899–925.
St-Maurice, J.P., Veronis, G., 1975. A multi-scaling analysis of the spin-up problem. J. Fluid Mech. 68, 417–445.
Sanders, T.M., Garvine, R.W., 2001. Fresh water delivery to the continental shelf and subsequent mixing. J. Geophys. Res. 106, 27,087-27,101.
Spall, M.A., Thomas, L.N., 2016. Downfront winds over buoyant coastal plumes. J. Phys. Oceanogr. 46, 3139–3154.
Thomas, L.N., Lee, C.M., 2005. Intensification of ocean fronts by down-front winds. J. Phys. Oceanogr. 35, 1086–1102.
Thomas, L.N., Taylor, J.R., 2010. Reduction of the useable wind-work on the general circulation by forced symmetric instability. Geophys. Res. Lett. 37, L18606 https://doi.org/10.1029/2010GL044680.
Weingartner, T.J., Danielson, S., Sasaki, Y., Pavlov, V., Kulakov, M., 1999. The Siberian Coastal Current: a wind-and buoyancy-forced Arctic coastal current. J. Geophys. Res. 104, 29,697-29,713.
Wijesekera, H.W., Allen, J.S., Newberger, P., 2003. A modeling study of turbulent mixing over the continental shelf: comparison of turbulent closure schemes. J. Geophys. Res. 108, 3103. https://doi.org/10.1029/2001JC001234.
Zhang, W.G., Gawarkiewicz, G.G., 2015. Length scale of the finite-amplitude meanders of shelfbreak fronts. J. Phys. Oceanogr. 45, 2598–2620.
Zhang, W.G., Lentz, S.J., 2017. Wind-driven circulation in a shelf valley. Part I: mechanism of the asymmetrical response to along-shelf winds in opposite directions. J. Phys. Oceanogr. 47, 2927–2947.